Nanoscale

PAPER

Cite this: *Nanoscale*, 2023, **15**, 7812

Excitation and emission distinguished photoluminescence enhancement in a plasmon–exciton intermediate coupling system†

Wenjun Zhang,[a,b] Long Gao,[b,c] Xiaohong Yan,[b,d] Hongxing Xu *[a,e] and Hong Wei *[b,f]

Received 14th December 2022,
Accepted 15th March 2023

DOI: 10.1039/d2nr07001d

rsc.li/nanoscale

Plasmonic nanocavities with tunable resonances provide a powerful platform to manipulate the light–matter interaction at the nanoscale. Here, we investigate the coupling between monolayer MoS_2 and the nanocavity formed by a silver nanowire (NW) and a gold film. The splitting of scattering spectra indicates intermediate coupling between the plasmon mode and two exciton states. The coupled system shows a photoluminescence (PL) intensity enhancement of 86-fold for the nanocavity with an appropriate NW diameter. In particular, the excitation and emission enhancement factors are experimentally distinguished, and the simulation results confirm the plasmon resonance dependent excitation and emission enhancements. Moreover, it is shown that the PL emission from the hybrid system becomes strongly polarized, and the degree of linear polarization larger than 0.9 is obtained. These results demonstrate the tunable coupling between plasmon mode and exciton states and help in deepening the understanding of the PL enhancement mechanisms.

Introduction

Plasmonic nanostructures can concentrate light into nanoscale volumes and thus largely enhance the local electromagnetic field and the local density of optical states, providing a versatile platform to manipulate light at the nanometer scale.[1,2] For quantum emitters coupling with plasmonic nanostructures, their spontaneous emission can be significantly modified.[3,4] The PL intensity of quantum emitters is jointly determined by the excitation rate, quantum yield, and collection efficiency. All these three parameters can be modified by coupling with surface plasmons. In addition to enhancing the emission intensity and accelerating the decay rate, plasmonic nanostructures can also tune the emission polarization,[5–8] providing various possibilities to manipulate the PL properties of quantum emitters and improve the performances of light-emitting devices. When the coupling strength is larger than the mean dissipation rate of the plasmons and excitons, the plasmon–exciton interaction enters into the strong coupling regime. The mixed states called plasmon–exciton polaritons or plexcitons are formed, which manifest as split peaks in optical spectra.[4,9,10] Plexciton states have been observed at room temperature in the coupled systems of plasmonic nanostructures and different types of quantum emitters, such as molecules,[11] J-aggregates,[12–14] quantum dots,[15–17] and two-dimensional transition metal dichalcogenides (TMDCs).[18–21]

In recent years, monolayer TMDCs have attracted much research interest owing to their exotic optical and optoelectronic properties.[22,23] Monolayer TMDCs possess direct band gap transitions, large binding energies, and high oscillator strengths. However, their intrinsically weak absorption and low PL quantum yield partly limit their application in future nanophotonic devices. The capability of plasmonic nanostructures to confine light into deep subwavelength volumes can dramatically improve the light absorption and emission performances of monolayer TMDCs. PL enhancement of monolayer TMDCs has been reported in several coupling systems, such as Au nanorods and WS_2,[24,25] Ag nanocubes on Au film and MoS_2 or WSe_2,[26–29] Ag NWs on Au film and $MoSe_2$,[30] Au nanospheres or nanosphere dimers on Au film

[a]*School of Physics and Technology, Center for Nanoscience and Nanotechnology, and Key Laboratory of Artificial Micro- and Nano-structures of Ministry of Education, Wuhan University, Wuhan 430072, China. E-mail: hxxu@whu.edu.cn*
[b]*Beijing National Laboratory for Condensed Matter Physics, Institute of Physics, Chinese Academy of Sciences, Beijing 100190, China. E-mail: weihong@iphy.ac.cn*
[c]*Institute of Microscale Optoelectronics, Shenzhen University, Shenzhen 518060, China*
[d]*School of Physical Sciences, University of Chinese Academy of Sciences, Beijing 100049, China*
[e]*School of Microelectronics, Wuhan University, Wuhan 430072, China*
[f]*Songshan Lake Materials Laboratory, Dongguan 523808, China*
† Electronic supplementary information (ESI) available. See DOI: https://doi.org/10.1039/d2nr07001d

and MoS_2,[31,32] and metal nanostructure arrays and MoS_2 or WSe_2.[33–36] Among a variety of plasmonic nanostructures, the coupled structure of a metal nanoparticle and a metal film is widely used, which is usually called nanoparticle-on-mirror (NPOM), due to its easy fabrication, ultrasmall mode volume, and readily tailored optical resonance over a wide spectral range.[37] In addition to PL enhancement, strong or intermediate coupling of the plasmon mode with one exciton state has been demonstrated in the coupled systems of NPOMs and monolayer TMDCs.[28–30,38–40] In spite of the progress, the strong coupling of multiple exciton states in monolayer TMDCs with plasmonic nanogap mode has not been explored yet. Moreover, while most studies were aimed to achieve a high PL enhancement factor, less effort has been devoted to experimentally disentangling the plasmon resonance dependent contributions of excitation enhancement and emission enhancement to the enhanced PL intensity.

Here, we utilize the plasmonic nanocavity formed by a silver NW on a gold mirror (named nanowire-on-mirror, NWOM) to manipulate the interaction between surface plasmons and excitons of monolayer MoS_2 at room temperature. The anticrossing dispersion curves obtained from the scattering spectra reveal the Rabi splitting of 121 meV and 105 meV for plasmons coupling with A exciton and B exciton, respectively. The PL intensity of A exciton of monolayer MoS_2 in the plasmonic nanocavity is enhanced by a factor of 86 compared with the MoS_2 on gold film, and the enhancement factor is dependent on the plasmon resonance wavelength that can be tuned by the NW diameter. By using two lasers of different wavelengths, we distinguish the excitation and emission enhancements in experiments. Theoretical simulations give further evidence for the contributions to the PL enhancement from the excitation and emission processes. In addition, the unpolarized PL of monolayer MoS_2 is converted to be linearly polarized when it is embedded in the plasmonic nanocavity. This hybrid system provides a versatile platform to tune plasmon–exciton coupling and PL emission.

Results and discussion

As illustrated in Fig. 1a, the coupled system is composed of monolayer MoS_2 inserted in the nanogap between a chemically synthesized Ag NW with a pentagonal cross-section and a Au film coated with an Al_2O_3 layer of 6 nm thickness (see section 1 in the ESI†). Fig. 1b shows the scanning electron microscopy (SEM) image of the MoS_2–NWOM coupled systems. The monolayer MoS_2 exhibited two clear exciton states A and B at ~658 nm (1.883 eV) and ~607 nm (2.043 eV) with a linewidth of 52 meV and 169 meV, respectively, as extracted from the differential reflection spectrum (Fig. 1c). A typical dark-field scattering spectrum of NWOM without monolayer MoS_2 shows two peaks (Fig. 1d). In the following studies, we focus on the plasmon mode at the longer wavelength. As shown in the inset of Fig. 1d, the electric field of this plasmon mode is confined in the nanogap between the Ag NW and the Au film and located around the corners of the NW (see also Fig. S1†).[41] It is noted that the scattering of this plasmon mode is polarized perpendicular to the NW (see Fig. S2†). Fig. 1e shows five dark-field scattering spectra of NWOMs with varying diameters of Ag NWs. As can be seen, the plasmon mode is progressively red-shifted with the increase of the NW diameter. The plasmon resonance energy is obtained by fitting the dark-field scattering spectra of NWOMs with one Lorentzian peak (the small peak at about 500 nm is cut off). The resonance wavelength converted from the resonance energy is approximately linearly proportional to the diameter of the NW, as shown in Fig. 1f. Therefore, by tuning the diameter of the NWs, certain plasmon resonance wavelengths can be obtained. The mean linewidth of the plasmon mode is about 279 meV (see Fig. S3†).

When the monolayer MoS_2 is sandwiched in the NWOM structure, peak splitting can be observed in the scattering spectra (Fig. 2a). Depending on the plasmon resonance energy, either A or B exciton alone or both can couple with the plasmon mode. The scattering spectra of MoS_2–NWOM coupled systems can be fitted by either two or three Lorentzian peaks, as shown in Fig. 2b. For the spectra fitted by three Lorentzian peaks, the three fitting peaks correspond to the energies of the lower plexciton branch (LPB, E_{LPB}), middle plexciton branch (MPB, E_{MPB}), and upper plexciton branch (UPB, E_{UPB}). The plasmon resonance energy E_{pl} can be obtained from $E_{pl} + E_A + E_B = E_{LPB} + E_{MPB} + E_{UPB}$, where E_A and E_B are the energies of A exciton and B exciton, respectively. The energies of three plexciton branches are plotted as a function of the plasmon resonance energy (circular dots in Fig. 2c). The solid curves in Fig. 2c are obtained by fitting the experimental plexciton energies using the model of three coupled oscillators (see section 5 in the ESI†), which show clear anticrossing behaviors. After the fitting, the peak energies of the scattering spectra fitted by two Lorentzian peaks are added to Fig. 2c as triangular dots. As can be seen, the triangular dots are also distributed close to the solid curves. This is because the dispersion curves are close to that of two coupled oscillators when the plasmon energy is close to one exciton state. If the plasmon energy is deduced from the linear relationship of the plasmon resonance wavelength and the NW diameter (Fig. 1f), similar results are obtained (see section 6 in the ESI†).

The coupling strengths of the plasmon mode with A exciton and B exciton are 65 meV and 57 meV, respectively. The minimal splitting between LPB and MPB and between MPB and UPB is about 121 meV and 105 meV, respectively. The minimal splitting between adjacent plexciton branches is smaller than the mean linewidth of two corresponding plexciton states (see section 7 in the ESI†), indicating that the coupling strength is in the intermediate coupling regime.[25,28,42] Fig. 2d shows the contributions of the plasmonic and two excitonic components for each plexciton branch obtained from the model of three coupled oscillators. For the UPB, the weight of A exciton is small, and the hybridization mainly depends on B exciton and the plasmon mode. B exciton dominates at the

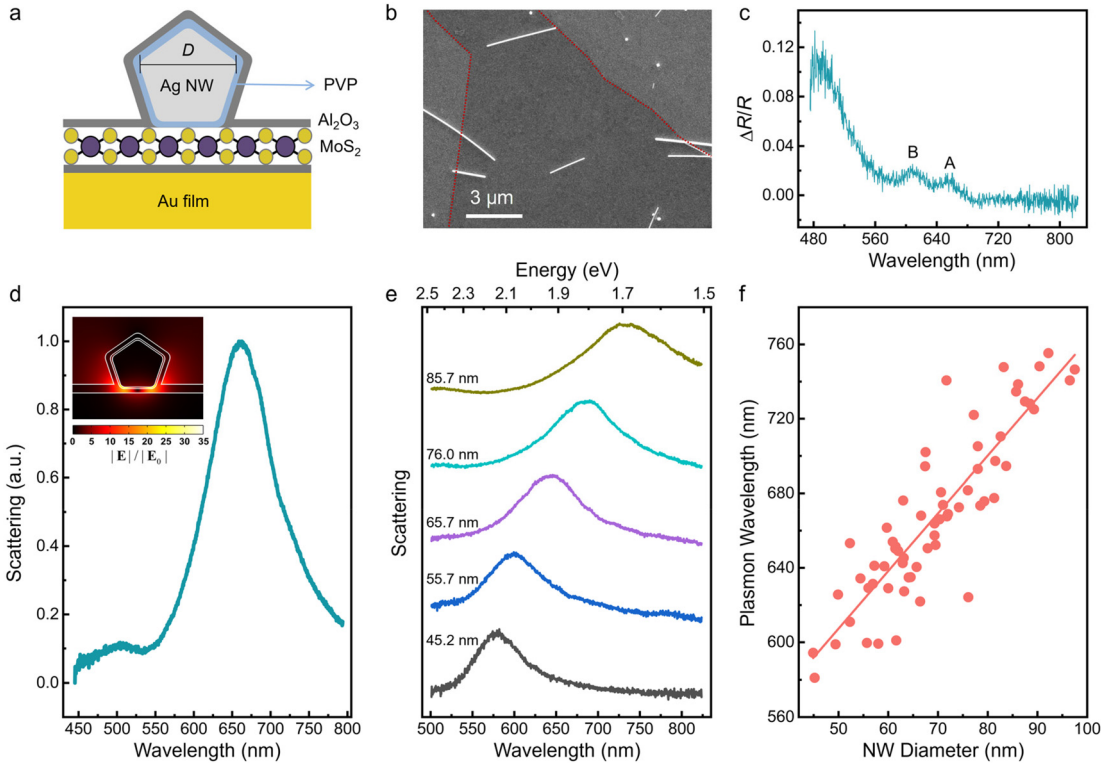

Fig. 1 Monolayer MoS_2-NWOM coupled system and characterization of MoS_2 and NWOMs. (a) Sketch of the cross-section of the coupled system. It consists of monolayer MoS_2 sandwiched between a Ag NW and a Au film, and Al_2O_3 is deposited on the Au film and on the top of the sample surface. *D* represents the NW diameter. (b) SEM image of the coupled systems. The monolayer MoS_2 is shown as the dark area with boundaries marked by red dashed lines. (c) Differential reflection spectrum of monolayer MoS_2 on Au film. (d) A representative dark-field scattering spectrum of the NWOM structure. The inset shows the electric field distribution of the plasmon mode with a NW diameter of 70 nm. (e) Normalized dark-field scattering spectra of individual NWOMs with the NW diameter increasing from bottom to top. The values of the NW diameter are written next to the corresponding spectra. (f) Plasmon resonance wavelength as a function of NW diameter. The solid line represents a linear fit.

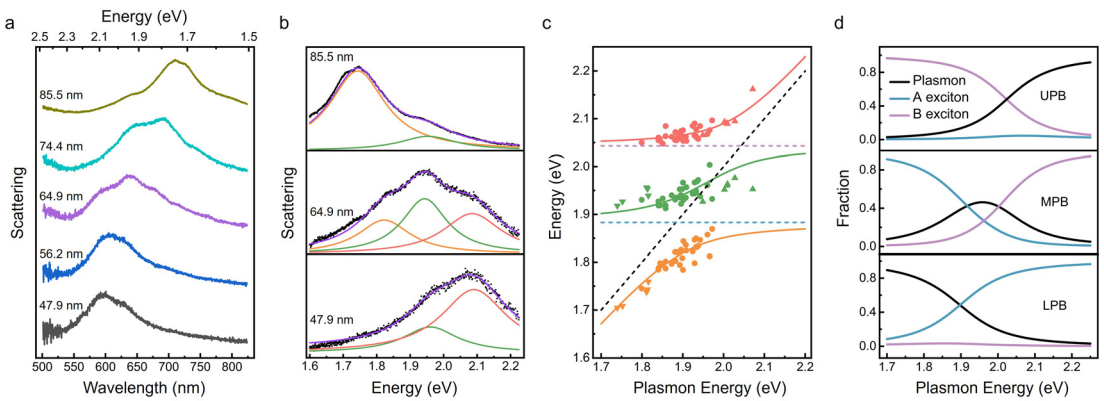

Fig. 2 Scattering spectra of monolayer MoS_2–NWOM coupled systems. (a) Normalized dark-field scattering spectra of MoS_2–NWOM coupled systems with the NW diameter increasing from bottom to top. (b) Scattering spectra fitted by two or three Lorentzian peaks, showing the evolution of plasmon mode coupling with A exciton (top), both A and B excitons (middle), and B exciton (bottom). The black dots show the experimental scattering spectra. The solid lines represent the Lorentzian fitting results. (c) Energies of plexciton branches as a function of plasmon energy. The red, green, and orange circular dots represent experimental UPB, MPB, and LPB of A exciton–plasmon–B exciton coupling, respectively. The red, green, and orange lines represent the fitting using the three-coupled-oscillators model. The green and orange inverted triangles represent experimental UPB and LPB of A exciton–plasmon coupling, respectively. The red and green upright triangles represent experimental UPB and LPB of B exciton–plasmon coupling, respectively. The blue and purple dashed lines indicate the energies of A exciton and B exciton, respectively. The black dashed line shows the plasmon energy obtained according to its relationship with the energies of plexcitons and excitons. (d) Fractions of the plasmon mode, A exciton, and B exciton for UPB, MPB, and LPB as a function of plasmon energy.

lower plasmon energy, while the plasmon mode dominates at the higher plasmon energy. Similarly, for the LPB, the hybridization mainly arises from the contributions of A exciton and the plasmon mode, and the plasmon mode dominates at the lower plasmon energy. For the MPB, both A and B excitons couple with the plasmon mode, forming the mixed state of three components.

Next, we investigated the PL enhancement of A exciton for monolayer MoS_2 in the NWOM nanocavity. Fig. 3a shows the PL spectra of a coupled system excited by laser light of two different wavelengths polarized perpendicular to the NW, together with the corresponding PL spectra of the MoS_2 on Au film without NW. Compared with the MoS_2 on Au film, the NWOM system shows higher PL intensities for both excitation wavelengths of 633 nm and 532 nm. Under the same excitation power, the PL intensity of the NWOM system is larger for 633 nm excitation. From the scattering spectrum in the inset of Fig. 3a, it can be seen that 633 nm is on resonance with one plexciton peak, while 532 nm is off resonance. Therefore, the excitation enhancement is larger for 633 nm excitation, which leads to a higher PL intensity compared with 532 nm excitation.

To quantitatively estimate the PL enhancement, we define the PL enhancement factor $\overline{EF}_{PL}$ as

$$\overline{EF}_{PL} = \frac{I_{NW} - \frac{A_0 - A_{NW}}{A_0} I_{MoS_2}}{I_{MoS_2}} \frac{A_0}{A_{NW}}, \quad (1)$$

where I_{NW} is the maximum intensity of the PL spectrum for the nanocavity system, I_{MoS_2} is the maximum PL intensity for the MoS_2 on Au film, A_0 represents the power of the focused laser beam within the collecting area, and A_{NW} is the power corresponding to the nanocavity area that is determined by the NW diameter and the collecting area. Fig. 3b shows the PL enhancement factor for 633 nm excitation as a function of the plasmon resonance wavelength of the NWOM system derived from the NW diameter. As can be seen, the PL enhancement factor is strongly dependent on the plasmon resonance wavelength. A maximum of 86-fold enhancement is achieved at the plasmon resonance wavelength of 678 nm. When the excitation wavelength is switched to 532 nm, the PL enhancement factor is decreased, but it still depends on the plasmon resonance wavelength, as shown in Fig. 3c. A maximum PL enhancement factor of 19 is obtained at the plasmon reso-

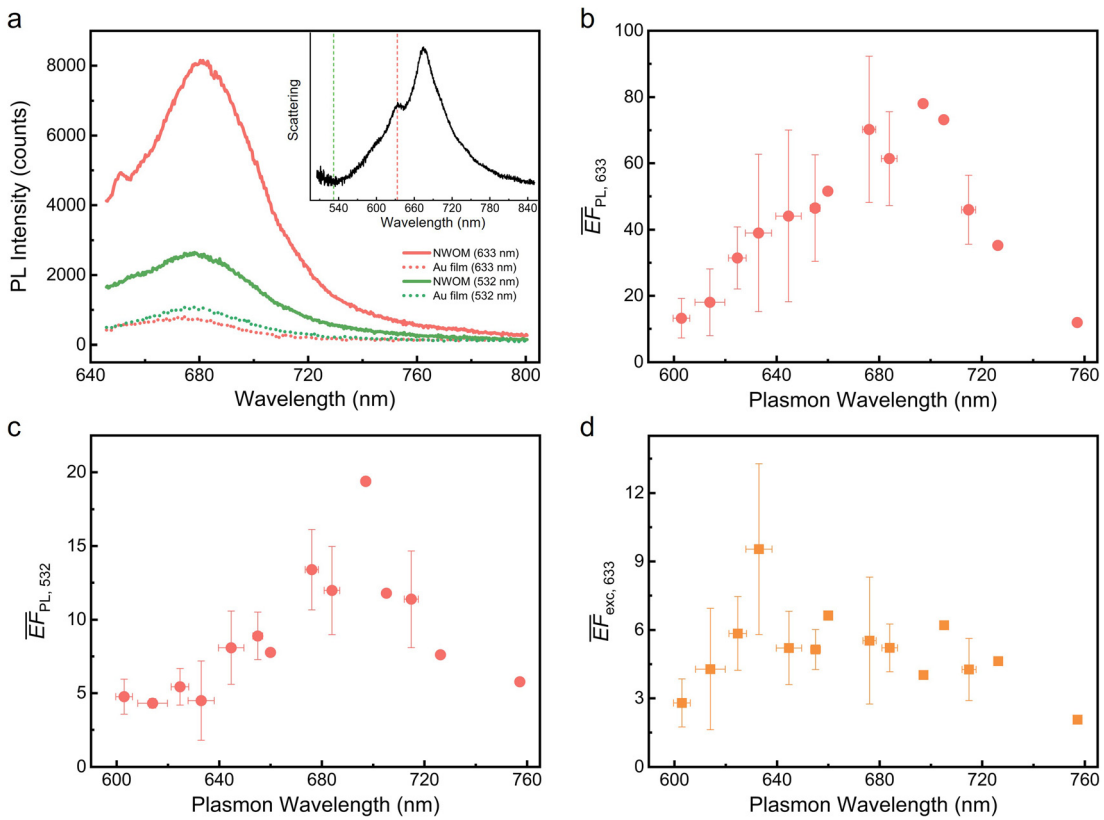

Fig. 3 Experimental PL enhancement of monolayer MoS_2–NWOM coupled systems. (a) PL spectra of MoS_2 coupled with NWOM (solid lines) and on Au film (dot lines) for excitation light of 633 nm (red) and 532 nm (green). The inset shows the corresponding scattering spectrum of the coupled system. The green and red vertical dashed lines indicate the excitation wavelength of 532 nm and 633 nm, respectively. (b and c) PL enhancement factor as a function of plasmon resonance wavelength for 633 nm excitation (b) and 532 nm excitation (c). (d) Derived excitation enhancement factor as a function of plasmon resonance wavelength for 633 nm excitation. The excitation light is polarized perpendicular to the NW. The dots with error bars are averaged values from two to nine coupled systems. The error bars represent the standard deviations (see also Fig. S6†).

nance wavelength of 697 nm. Since 532 nm laser light is off resonance with the coupled system, the excitation enhancement is negligible, which is confirmed by the simulations in the latter part. Therefore, the PL enhancement is mainly from the emission enhancement. Since the emission enhancement is independent of the excitation laser wavelength and relies on the emission wavelength and the antenna structure only, the PL for both excitation wavelengths shares the same emission enhancement factor. The PL enhancement factor for 532 nm excitation can be approximated as the emission enhancement factor. Then, the excitation enhancement factor for 633 nm excitation can be obtained from the approximate relationship:

$$\overline{EF}_{\mathrm{exc},633} \approx \overline{EF}_{\mathrm{PL},633}/\overline{EF}_{\mathrm{PL},532}, \quad (2)$$

where $\overline{EF}_{\mathrm{exc},633}$ is the excitation enhancement factor for 633 nm excitation light, and $\overline{EF}_{\mathrm{PL},633}$ and $\overline{EF}_{\mathrm{PL},532}$ are the PL enhancement factors for excitation light of 633 nm and 532 nm, respectively. Fig. 3d shows the derived excitation enhancement factor for 633 nm excitation wavelength (see also Fig. S6†). The maximum value of 13 is reached at the plasmon resonance wavelength of ~630 nm, which is close to the excitation wavelength. To further confirm that the plasmon resonance contributes to the PL enhancement, we also performed PL measurements with the excitation light polarized parallel to the NW. Under such circumstances, the plasmon mode cannot be excited and the PL intensity of the NWOM system appears to have no significant enhancement compared with the MoS_2 on Au film for both 633 nm and 532 nm excitation (Fig. S7†).

To further understand the experimental results, simulations by the finite element method were performed with structural and optical parameters mimicking experimental conditions (see section 9 in the ESI†). Fig. 4a shows the scattering spectra of the NWOM nanocavity with monolayer MoS_2 for different NW diameters. Compared with the scattering spectra of NWOMs without MoS_2 (Fig. S8†), peak splitting is observed near the wavelength of A exciton. Fig. 4b and c show the calculated excitation and PL enhancement factors for excitation wavelengths of 532 nm and 633 nm, respectively, together with the emission enhancement factor. As shown by the green triangles in Fig. 4b and c, the emission enhancement reaches the maximum for the NW diameter of 70 nm, corresponding to a plasmon resonance wavelength close to the PL emission wavelength. For the excitation wavelength of 532 nm, the enhancement factor of excitation is very small, and the PL enhancement factor is close to the emission enhancement factor (Fig. 4b). For 633 nm excitation, the excitation enhancement gets to the maximum for the nanocavity with a NW diameter of 57.5 nm (orange squares in Fig. 4c), which possesses a plasmon resonance wavelength close to the excitation wavelength. The maximum PL enhancement is obtained for the nanocavity with a NW diameter of 67.5 nm (red dots in Fig. 4c), which benefits from both the excitation and emission enhancements. Compared to the experimental results, the simulated results show similar trends of the dependence of enhancement factor on the plasmon resonance wavelength.

Finally, we measured the polarization of the PL emission from the coupled system. The excitation light of 633 nm wavelength is polarized perpendicular to the NW. As shown in Fig. 5a, the intensity of PL polarized perpendicular to the NW is significantly higher than that of PL polarized parallel to the NW. Fig. 5b shows the maximum PL intensities in polar plots with the polarization angle varying from 0° to 360°. 0° is defined as the direction corresponding to the polarization parallel to the NW. For the monolayer MoS_2 on Au film (red dots in Fig. 5b), the PL is unpolarized and the intensity is almost identical for different polarization directions due to the valley decoherence at room temperature.[43,44] For the monolayer MoS_2-NWOM system, the PL becomes linearly polarized perpendicular to the NW (black squares in Fig. 5b). To quantitatively analyze the polarization of the PL, the degree of linear polarization (DOLP) is calculated as DOLP = $(I_\perp - I_{/\!/})/(I_\perp + I_{/\!/})$, where $I = I_{\mathrm{NW}} - I_{\mathrm{MoS_2}}(A_0 - A_{\mathrm{NW}})/A_0$ represents the PL intensity from the monolayer MoS_2 in the NWOM nanocavity, and the subscripts $\perp$ and // represent the PL polarized perpendicular and parallel to the NW, respectively. The experimental results are plotted as a function of the plasmon resonance wavelength (Fig. 5c). The DOLP larger than 0.9 is obtained around a plasmon resonance wavelength of 680 nm, indicating that the PL from the monolayer MoS_2 coupled with NWOM becomes linearly polarized. The calculated results for the DOLP are shown in Fig. 5d, agreeing well with the experimental results. The large DOLP for the PL of the coupled system is because

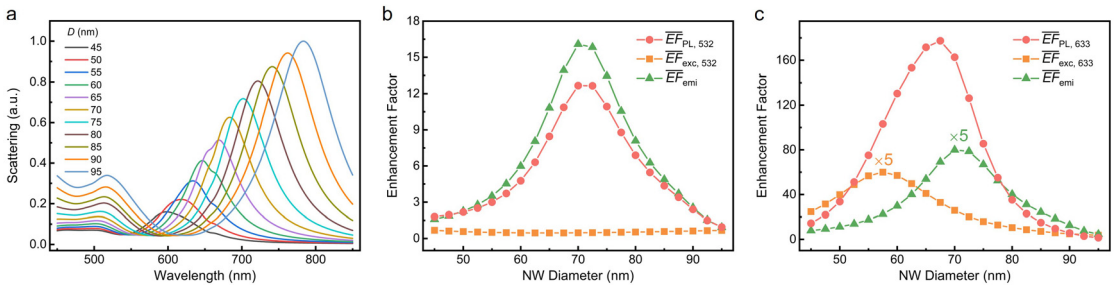

Fig. 4 Simulation results for MoS_2–NWOM coupled systems. (a) Scattering spectra of the coupled systems with different NW diameters D. (b and c) PL (red dots), excitation (orange squares), and emission (green triangles) enhancement factors as a function of NW diameter for 532 nm excitation (b) and 633 nm excitation (c). The excitation and emission enhancement factors in (c) are magnified five times.

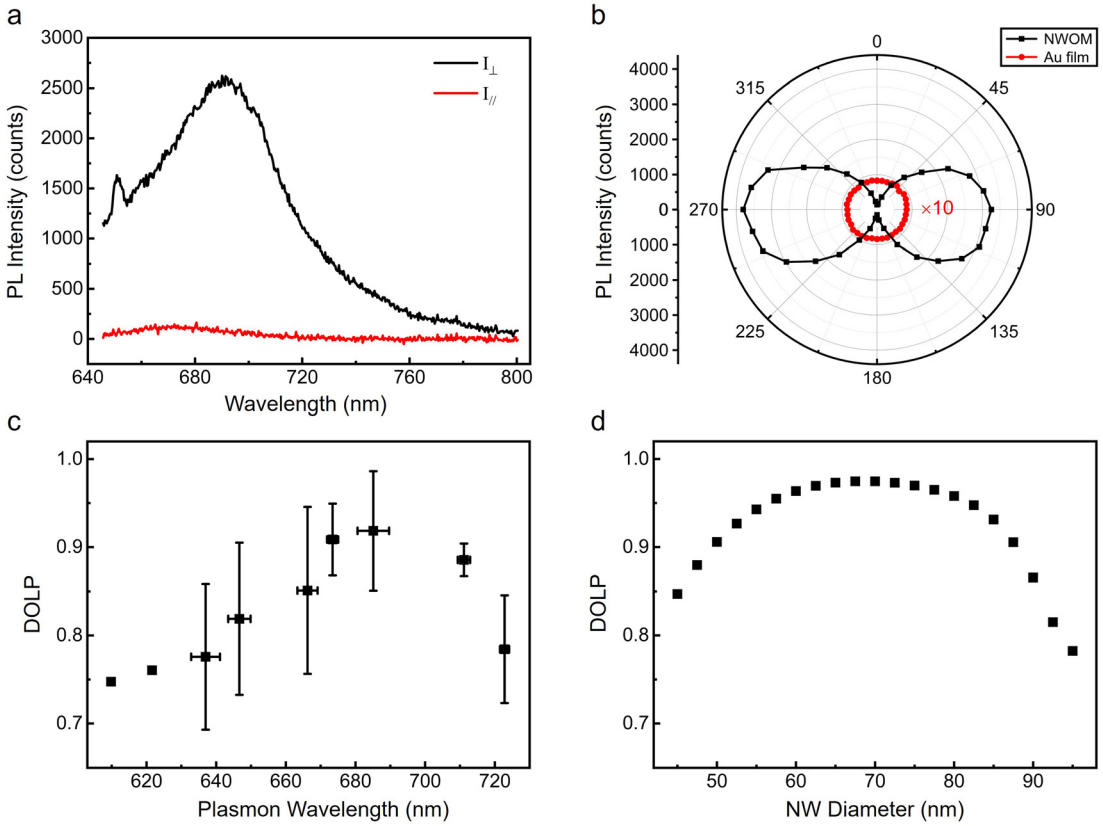

Fig. 5 PL polarization of monolayer MoS_2–NWOM coupled systems. (a) PL spectra of a coupled system for the emission polarization perpendicular (black line) and parallel (red line) to the NW. (b) Polar plots of the maximum PL intensity from MoS_2–NWOM (black squares) and MoS_2 on Au film (red dots) for different emission polarizations. 0° corresponds to the polarization parallel to the NW, and the PL spectra are measured with the polarization angle increasing from 0° to 360° at intervals of 10°. (c) Experimental results of DOLP as a function of plasmon resonance wavelength. The squares with error bars are averaged values from two to six coupled systems. The error bars represent the standard deviations. (d) Calculated DOLP as a function of NW diameter. For both the experimental and simulated results, the excitation light is of 633 nm wavelength and polarized perpendicular to the NW.

the plasmon resonance dependent enhancement of PL intensity is contributed dominantly by the dipoles oriented perpendicular to the NW (see Fig. S13 and S15†). This polarization behavior can also be qualitatively understood by the efficient energy transfer from the excitons of MoS_2 to the plasmon mode of NWOM, the radiation of which is linearly polarized perpendicular to the NW.[6]

Conclusion

We have demonstrated the intermediate coupling of one plasmon mode with one or two exciton states, plasmon resonance dependent PL enhancement, and linearly polarized PL emission in the coupled system of monolayer MoS_2 and NWOM. By tuning the plasmon resonance wavelength, both A exciton and B exciton or one of them can strongly interact with the plasmon mode, inducing peak splitting in the dark-field scattering spectra. The PL emission of A exciton is enhanced by the NWOM, and the enhancement factor strongly depends on the plasmon resonance wavelength. The excitation enhancement and emission enhancement are distinguished in experiments by using two excitation lasers with the wavelength on or off resonance with the plasmon mode. Additionally, it is shown that the PL from the coupled system becomes linearly polarized in a wide range of NW diameters. This study provides a highly tunable platform to manipulate plasmon–exciton coupling, reveals the plasmon resonance dependent PL emission properties, and will inspire new designs of plasmon–exciton coupling systems for room-temperature nanophotonic devices.

Conflicts of interest

The authors declare no competing financial interest.

Acknowledgements

This work was supported by the National Key R&D Program of China (Grant No. 2021YFA1201500 and 2021YFA1401100), the National Natural Science Foundation of China (Grant No.

12074421 and 91850207), and the Strategic Priority Research Program of Chinese Academy of Sciences (Grant No. XDB33000000). We thank Yijie Niu for the help in analyzing the data and Li Chen for the helpful discussions about the simulations. We thank the Laboratory of Microfabrication at the Institute of Physics, Chinese Academy of Sciences for experimental support.

References

1 J. A. Schuller, E. S. Barnard, W. Cai, Y. C. Jun, J. S. White and M. L. Brongersma, *Nat. Mater.*, 2010, **9**, 193–204.
2 J. J. Baumberg, J. Aizpurua, M. H. Mikkelsen and D. R. Smith, *Nat. Mater.*, 2019, **18**, 668–678.
3 M. Pelton, *Nat. Photonics*, 2015, **9**, 427–435.
4 H. Wei, X. H. Yan, Y. J. Niu, Q. Li, Z. L. Jia and H. X. Xu, *Adv. Funct. Mater.*, 2021, **31**, 2100889.
5 Z. P. Li, T. Shegai, G. Haran and H. X. Xu, *ACS Nano*, 2009, **3**, 637–642.
6 T. Ming, L. Zhao, H. J. Chen, K. C. Woo, J. F. Wang and H. Q. Lin, *Nano Lett.*, 2011, **11**, 2296–2303.
7 J. W. Tang, J. Xia, M. D. Fang, F. L. Bao, G. J. Cao, J. Q. Shen, J. L. Evans and S. L. He, *Nat. Commun.*, 2018, **9**, 1705.
8 G. P. Zhu, X. Q. Shi, G. Y. Huang, K. Z. Liu, W. Wei, Q. Q. Guo, W. Du and T. Wang, *Adv. Opt. Mater.*, 2022, **10**, 2101762.
9 P. Törmä and W. L. Barnes, *Rep. Prog. Phys.*, 2015, **78**, 013901.
10 D. G. Baranov, M. Wersall, J. Cuadra, T. J. Antosiewicz and T. Shegai, *ACS Photonics*, 2018, **5**, 24–42.
11 R. Chikkaraddy, B. de Nijs, F. Benz, S. J. Barrow, O. A. Scherman, E. Rosta, A. Demetriadou, P. Fox, O. Hess and J. J. Baumberg, *Nature*, 2016, **535**, 127–130.
12 A. E. Schlather, N. Large, A. S. Urban, P. Nordlander and N. J. Halas, *Nano Lett.*, 2013, **13**, 3281–3286.
13 G. Zengin, M. Wersäll, S. Nilsson, T. J. Antosiewicz, M. Käll and T. Shegai, *Phys. Rev. Lett.*, 2015, **114**, 157401.
14 R. M. Liu, Z. K. Zhou, Y. C. Yu, T. W. Zhang, H. Wang, G. H. Liu, Y. M. Wei, H. J. Chen and X. H. Wang, *Phys. Rev. Lett.*, 2017, **118**, 237401.
15 K. Santhosh, O. Bitton, L. Chuntonov and G. Haran, *Nat. Commun.*, 2016, **7**, 11823.
16 H. X. Leng, B. Szychowski, M. C. Daniel and M. Pelton, *Nat. Commun.*, 2018, **9**, 4012.
17 J. Y. Li, W. Li, J. Liu, J. Zhong, R. M. Liu, H. J. Chen and X. H. Wang, *Nano Lett.*, 2022, **22**, 4686–4693.
18 D. Zheng, S. P. Zhang, Q. Deng, M. Kang, P. Nordlander and H. X. Xu, *Nano Lett.*, 2017, **17**, 3809–3814.
19 J. X. Wen, H. Wang, W. L. Wang, Z. X. Deng, C. Zhuang, Y. Zhang, F. Liu, J. C. She, J. Chen, H. J. Chen, S. Z. Deng and N. S. Xu, *Nano Lett.*, 2017, **17**, 4689–4697.
20 X. H. Yan and H. Wei, *Nanoscale*, 2020, **12**, 9708–9716.
21 Y. J. Niu, H. X. Xu and H. Wei, *Phys. Rev. Lett.*, 2022, **128**, 167402.
22 Q. H. Wang, K. Kalantar-Zadeh, A. Kis, J. N. Coleman and M. S. Strano, *Nat. Nanotechnol.*, 2012, **7**, 699–712.
23 A. Krasnok, S. Lepeshov and A. Alú, *Opt. Express*, 2018, **26**, 15972–15994.
24 J. Kern, A. Trügler, I. Niehues, J. Ewering, R. Schmidt, R. Schneider, S. Najmaei, A. George, J. Zhang, J. Lou, U. Hohenester, S. Michaelis de Vasconcellos and R. Bratschitsch, *ACS Photonics*, 2015, **2**, 1260–1265.
25 Y. Z. Jiang, H. Wang, S. Y. Wen, H. J. Chen and S. Z. Deng, *ACS Nano*, 2020, **14**, 13841–13851.
26 G. M. Akselrod, T. Ming, C. Argyropoulos, T. B. Hoang, Y. X. Lin, X. Ling, D. R. Smith, J. Kong and M. H. Mikkelsen, *Nano Lett.*, 2015, **15**, 3578–3584.
27 J. Huang, G. M. Akselrod, T. Ming, J. Kong and M. H. Mikkelsen, *ACS Photonics*, 2018, **5**, 552–558.
28 J. W. Sun, H. T. Hu, D. Zheng, D. X. Zhang, Q. Deng, S. P. Zhang and H. X. Xu, *ACS Nano*, 2018, **12**, 10393–10402.
29 S. Y. Hou, L. Y. M. Tobing, X. L. Wang, Z. W. Xie, J. H. Yu, J. Zhou, D. H. Zhang, C. Dang, P. Coquet, B. K. Tay, M. D. Birowosuto, E. H. T. Teo and H. Wang, *Adv. Opt. Mater.*, 2019, **7**, 1900857.
30 C. Y. Li, Q. F. Wang, H. Diao, Z. Hao, W. X. Yu, K. H. Liu, X. T. Gan, F. J. Xiao and J. L. Zhao, *Laser Photonics Rev.*, 2022, **16**, 2100199.
31 X. Z. Qi, T. W. Lo, D. Liu, L. T. Feng, Y. Chen, Y. K. Wu, H. L. Ren, G. C. Guo, D. Y. Lei and X. F. Ren, *Nanophotonics*, 2020, **9**, 2097–2105.
32 S. Y. Cao, L. P. Hou, Q. F. Wang, C. Y. Li, W. X. Yu, X. T. Gan, K. H. Liu, M. Premaratne, F. J. Xiao and J. L. Zhao, *Photonics Res.*, 2021, **9**, 501–506.
33 B. Lee, J. Park, G. H. Han, H. S. Ee, C. H. Naylor, W. J. Liu, A. T. C. Johnson and R. Agarwal, *Nano Lett.*, 2015, **15**, 3646–3653.
34 Z. Wang, Z. G. Dong, Y. H. Gu, Y. H. Chang, L. Zhang, L. J. Li, W. J. Zhao, G. Eda, W. J. Zhang, G. Grinblat, S. A. Maier, J. K. W. Yang, C. W. Qiu and A. T. S. Wee, *Nat. Commun.*, 2016, **7**, 11283.
35 H. H. Su, S. Wu, Y. H. Yang, Q. Leng, L. Huang, J. Q. Fu, Q. J. Wang, H. Liu and L. Zhou, *Nanophotonics*, 2020, **10**, 975–982.
36 M. W. Yu, S. Ishii, S. S. Li, J. R. Ku, J. H. Yang, K. L. Su, T. Taniguchi, T. Nagao and K. P. Chen, *npj 2D Mater. Appl.*, 2021, **5**, 47.
37 G. C. Li, Q. Zhang, S. A. Maier and D. Y. Lei, *Nanophotonics*, 2018, **7**, 1865–1889.
38 X. B. Han, K. Wang, X. Y. Xing, M. Y. Wang and P. X. Lu, *ACS Photonics*, 2018, **5**, 3970–3976.
39 J. Qin, Y. H. Chen, Z. P. Zhang, Y. F. Zhang, R. J. Blaikie, B. Y. Ding and M. Qiu, *Phys. Rev. Lett.*, 2020, **124**, 063902.
40 X. Z. Liu, J. Yi, S. Yang, E. C. Lin, Y. J. Zhang, P. Y. Zhang, J. F. Li, Y. Wang, Y. H. Lee, Z. Q. Tian and X. Zhang, *Nat. Mater.*, 2021, **20**, 1210–1215.
41 W. Chen, S. P. Zhang, Q. Deng and H. X. Xu, *Nat. Commun.*, 2018, **9**, 801.

42 Y. J. Niu, L. Gao, H. X. Xu and H. Wei, *Nanophotonics*, 2023, **12**, 735–742.
43 H. L. Zeng, J. F. Dai, W. Yao, D. Xiao and X. D. Cui, *Nat. Nanotechnol.*, 2012, **7**, 490–493.
44 A. M. Jones, H. Y. Yu, N. J. Ghimire, S. F. Wu, G. Aivazian, J. S. Ross, B. Zhao, J. Q. Yan, D. G. Mandrus, D. Xiao, W. Yao and X. D. Xu, *Nat. Nanotechnol.*, 2013, **8**, 634–638.